

# Lab on a Chip

Accepted Manuscript



This is an *Accepted Manuscript*, which has been through the Royal Society of Chemistry peer review process and has been accepted for publication.

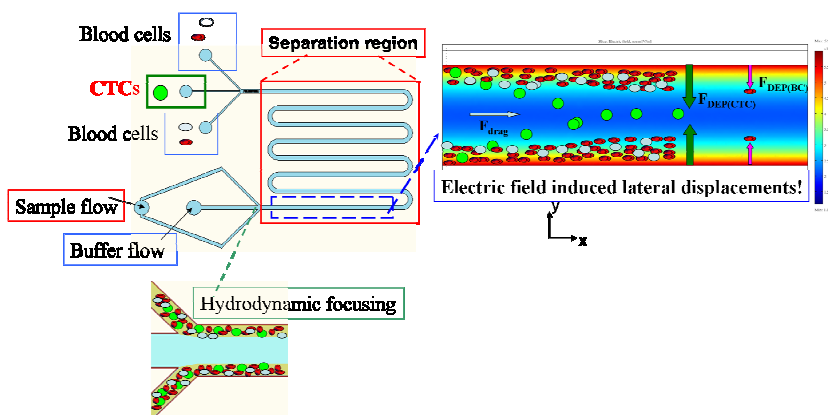
*Accepted Manuscripts* are published online shortly after acceptance, before technical editing, formatting and proof reading. Using this free service, authors can make their results available to the community, in citable form, before we publish the edited article. We will replace this *Accepted Manuscript* with the edited and formatted *Advance Article* as soon as it is available.

You can find more information about *Accepted Manuscripts* in the [Information for Authors](#).

Please note that technical editing may introduce minor changes to the text and/or graphics, which may alter content. The journal's standard [Terms & Conditions](#) and the [Ethical guidelines](#) still apply. In no event shall the Royal Society of Chemistry be held responsible for any errors or omissions in this *Accepted Manuscript* or any consequences arising from the use of any information it contains.

## Table of content

We present an antibody-free approach for high throughput and purity dielectrophoretic isolation of CTCs from blood in a microfluidic chip.



1 Antibody-Free Isolation of Rare Cancer Cells from Blood based  
2 on 3D Lateral Dielectrophoresis

3

4 I-Fang Cheng<sup>1\*</sup>, Wei-Lung Huang<sup>2</sup>, Tzu-Ying Chen<sup>1</sup>, Chien-Wei Liu<sup>3</sup>, Yu-De Lin<sup>1</sup>,  
5 Wu-Chou Su<sup>2,4\*</sup>

6

7

8 <sup>1</sup>*National Nano Device Laboratories, National Applied Research Laboratories,*  
9 *Tainan, Taiwan*

10 <sup>2</sup>*Department of Internal Medicine, National Cheng Kung University College of*  
11 *Medicine and Hospital, Tainan, Taiwan*

12 <sup>3</sup>*Department of Mechanical Engineering, National Yunlin University of Science*  
13 *and Technology, Yunlin, Taiwan*

14 <sup>4</sup>*Cancer Center, National Cheng Kung University Hospital, Tainan, Taiwan*

15

16

17

18

19

20

21

22 \*Corresponding Author:

23 I-Fang Cheng

24 E-mail: [ifcheng@narlabs.org.tw](mailto:ifcheng@narlabs.org.tw)

25

26 Wu-Chou Su:

27 E-mail: [sunnysu@mail.ncku.edu.tw](mailto:sunnysu@mail.ncku.edu.tw)

28

29

30

31

32

**1 Abstract**

2 We present an antibody-free approach for the high-purity and high-throughput  
3 dielectrophoretic (DEP) isolation of circulating tumour cells (CTCs) from blood in a  
4 microfluidic chip. A hydrodynamic sheath flow is designed upstream in the chip to  
5 focus the suspension samples to the channel side walls, thus providing a queue to  
6 allow DEP-induced lateral displacements. High-throughput continuous cancer cell  
7 sorting (maximum flow rate: ~2.4 mL/h, linear velocity: ~4 mm/s) is achieved with a  
8 sustained 3D lateral DEP (LDEP) particle force normal to the continuous  
9 through-flow. This design allows the continuous fractionation of micro-/nanosized  
10 particles into different downstream subchannels based on the differences in their  
11 different critical negative DEP strengths/mobilities. The main advantage of this  
12 separation strategy is that increasing the channel length can effectively increase the  
13 throughput proportionally. The effective separation of rare cancer cells (<0.001%)  
14 from diluted human blood in a handheld chip is demonstrated. An enrichment factor  
15 of  $10^5$  and recovery rate of ~85% from a 0.001% cancer cell sample is achieved at an  
16 optimal flow rate of 20  $\mu\text{L}/\text{min}$  passing through a 6-cm-long LDEP channel and an  
17 appropriate voltage at a frequency of 10 kHz. A higher throughput of 2.4 mL/h is also  
18 achieved with a 13-cm-long metal-based microchannel.

19 **Key words:** isolation, circulating tumour cells, dielectrophoresis

## 1 **Introduction**

2 Cancer cells that detach from a tumour, enter blood vessels, and circulate in  
3 the circulatory system are called circulating tumour cells (CTCs). CTCs can be used  
4 for the in-vitro diagnosis and assessment of cancers/tumours<sup>1</sup>. CTCs can provide a  
5 considerable amount of real-time information for cancer diagnoses such as localized  
6 cancer identification, drug susceptibility assessment, therapeutic monitoring, and  
7 prognosis assessment/tracking<sup>2</sup>. Furthermore, the number of CTCs can be used to  
8 evaluate the cancer prognosis and relapse, making it possible to predict cancer  
9 progression<sup>3</sup>. Therefore, there is a strong need for the early detection and assessment  
10 of CTCs, because this can enable early treatment. However, before analyses such as  
11 cell counting, prognosis and metastasis assessment, and identification of localized  
12 tumour cells can be conducted, it is very important to ensure the high recovery  
13 isolation of CTCs from blood.

14 The density gradient centrifugation method is used most commonly to isolate  
15 target cells from a heterogeneous medical sample<sup>4</sup>. However, this method fails in the  
16 case of low purity, recovery rate, and cell viability, as these conditions do not meet the  
17 requirements for further analysis and assessment. Alternatively, large, expensive  
18 equipment and the use of flow cytometry have been successfully used for isolating  
19 and counting CTCs using fluorescence- or magnetic-bead-based cell sorting systems<sup>5</sup>.

1   <sup>6</sup>. However, such platforms limit the success rate of separating CTCs and further  
2   applications owing to the laborious sample preparations involved, which introduce  
3   artifacts or lead to the loss of the desired cells.

4        Antibody-based methods have proved popular for specifically capturing CTCs.  
5   In these methods, CTCs are captured using specific tumour antibodies such as  
6   epithelial-specific cell adhesion molecule (EpCAM) and cytokeratins (CKs)<sup>7, 8</sup>.  
7   Microfluidics and BioMEMS technologies have enabled low-cost, portable, and  
8   automatic operation as well as higher efficiency of antibody-specific binding for CTC  
9   isolation owing to their high surface-to-volume ratio<sup>9, 10</sup>. Biomarker-based isolation  
10  methods such as a modified antibody in a micropillar array<sup>10-12</sup> and nanoroughened  
11  surfaces in a microfluidic channel<sup>13</sup> have been developed to specifically capture CTCs  
12  in a microfluidic chip. Furthermore, immunomagnetic bead-based systems have been  
13  used for the isolation of CTCs and subsequent culture of rare CTCs in a microfluidic  
14  chip<sup>14</sup>. Unfortunately, some CTCs may show low or no EpCAM/CK expression on  
15  the cell membrane, and therefore, they cannot be effectively captured using the  
16  proposed biomarkers<sup>15, 16</sup>. Furthermore, the use of expensive antibodies results in  
17  additional costs related to detection and time consumption in  
18  conjugation/immobilization processes (typically 4–8 h).

19        In contrast, antibody-free approaches isolate CTCs without relying on antibodies

1 or biomarkers for specifically capturing tumour cells. Instead, they isolate cells based  
2 on different physical properties such as size, dielectric properties, and shapes intrinsic  
3 to cancer cells and blood cells<sup>17, 18</sup>. Microfluidic filters and membranes capture CTCs  
4 by size selection<sup>19, 20</sup>. Nevertheless, cell clogging limits their success, and high shear  
5 stress on the cell surface could significantly influence the cell viability during  
6 filtration<sup>20</sup>. Hydrodynamic mechanisms, such as inertial force and centrifuge force in  
7 a microchannel design, have been developed over the last few years to achieve size  
8 separation based on the size difference between CTCs and blood cells<sup>21-23</sup>. However,  
9 the purity of the isolated CTCs is relatively low (0.5%–10%) when the sample purity  
10 is lower than 0.1%<sup>24</sup>.

11 Dielectrophoresis (DEP) provides more effective and flexible (real-time  
12 controllable) separation based on the size and dielectric properties<sup>24-26</sup>. Noncontact  
13 DEP approaches can also reduce cell damage, thus increasing the possibility of further  
14 analysis and assessment. Several strategies such as DEP gates<sup>27-29</sup>, light-induced DEP  
15 (LIDEP)<sup>30, 31</sup>, side-wall DEP<sup>32</sup>, traveling-wave DEP (twDEP)<sup>33, 34</sup>, and DEP-field flow  
16 fraction (DEP-FFF)<sup>35</sup> have been reported to precisely separate particles based on size  
17 using the DEP force as a function of particle volume  $r^3$ . In general, the DEP force can  
18 only affect local particles in short range because the decay relation of the electric field  
19 depends on the electrode shape and distance. For large distances relative to the

1 electrode size, the field strength decays with  $d^{-1}$  for a distant counter electrode. For a  
2 2D planar electrode configuration, too, the electric field decays exponentially with the  
3 distance from the electrodes along the z-direction<sup>25</sup>, thus causing particle separation to  
4 be characterized by a short range and low throughput (0.1–3  $\mu\text{L}/\text{min}$ )<sup>17, 36</sup>.  
5 High-throughput and high-purity separation is required for CTC isolation because the  
6 number of CTCs is generally relatively low compared to the number of blood cells  
7 (1–10000 CTCs/mL in human blood, i.e.,  $10^{-3}\%$  to  $10^{-7}\%$  of the total number of cells  
8 in blood). Therefore, short-range DEP separation designs cannot meet the  
9 requirements of practical applications.

10 In this study, we propose an antibody-free and long-range 3D DEP microfluidic  
11 platform for the effective and high-throughput isolation of rare cancer cells from  
12 diluted human blood. Our design uses a V-shaped microchannel with a long-range  
13 electric field gradient that induces a lateral DEP (LDEP) force normal to the  
14 continuous through-flow, as shown in Figure 1(a). This mechanism provides a long  
15 residence time for dielectrophoretically manipulating CTCs and blood cells to their  
16 specific equilibrium positions in the microchannel. Bioparticles with different sizes,  
17 dielectric properties, and shapes show different LDEP velocities and equilibrium  
18 positions, resulting in the sorting of CTCs and blood cells to different downstream  
19 subchannels with high throughputs. The throughput of the LDEP chip could be 1–2



1 orders higher than that of conventional gate/barrier-based DEP separators (0.1–3  
 2  $\mu\text{L}/\text{min}$ )<sup>28, 30, 32</sup>. As a proof-of-concept, PC14PE6/AS2-GFP (AS2-GFP) lung cancer  
 3 cells were spiked into human blood to demonstrate the capability to isolate CTCs. The  
 4 equilibrium position of the DEP force and the frequency-dependent LDEP migration  
 5 rate for tumour cells and blood cells were investigated to optimize the separation  
 6 conditions. The effective separation of rare cancer cells from diluted human blood in  
 7 the chips is successfully demonstrated. To the best of our knowledge, no study has  
 8 previously reported the use of a 3D long-range LDEP force normal to the continuous  
 9 through-flow to achieve the high-throughput and high-purity isolation of CTCs.

10

## 11 **Materials and Methods**

### 12 **Theory and chip design**

13 DEP is the induced motion of a polarized dielectric particle by a nonuniform AC  
 14 electric-field-induced polarization. The time-averaged DEP force is defined as

$$15 \quad F_{DEP} = 2\pi r^3 \varepsilon_m \text{Re}[f_{CM}(\omega)] \nabla E^2 \quad (1)$$

16 where  $\varepsilon_m$  is the permittivity of the medium;  $r$ , the radius of the particle; and  $\nabla E^2$ ,  
 17 the magnitude of the electric field gradient. The effective polarizability-  
 18 Clausius-Mossotti (CM) factor  $f_{CM}$  is given by

$$19 \quad f_{CM} = \frac{\varepsilon_p^* - \varepsilon_m^*}{\varepsilon_p^* + 2\varepsilon_m^*} \quad (2)$$

1  $\epsilon_p^*$  and  $\epsilon_m^*$  indicate the complex permittivity of the particle and the surrounding  
 2 medium, respectively. The effect of the complex permittivity can be controlled by  
 3 changing the frequency ( $\omega$ ) of the applied electric field and can be given as  $\epsilon^* = \epsilon -$   
 4  $i(\sigma/\omega)$ . If particles are more or less polarizable than the surrounding medium, they  
 5 will be moved to a region with relatively strong (positive DEP) or relatively weak  
 6 (negative DEP) electrical field gradient, respectively. When an AC electric field is  
 7 imposed on a cell suspended in a medium having much lower conductivity than the  
 8 cell cytoplasm,  $f_{CM}$  may be approximated as<sup>37, 38</sup>

$$9 \quad f_{CM} = \frac{f_1^2 - f_{co}^2}{f_1^2 + 2f_{co}^2} \quad (3)$$

10  $f_1$  represents the applied AC electric frequency and  $f_{co}$ , the crossover frequency (no  
 11 particle DEP movements,  $\text{Re}[f_{CM}] = 0$ ). At sufficiently high frequency ( $f > \sigma_m/C_{mem}$ ),  
 12 the electric field can penetrate the cell membrane and the cytoplasm. The internal  
 13 cytoplasmic conductivity of the cell, which is related to the external medium's  
 14 conductivity, significantly influences the crossover frequency of a cell.  $f_{co}$  can be  
 15 given as

$$16 \quad f_{co} = \frac{1}{2\pi r C_{mem}} \sqrt{\frac{2\sigma_p \sigma_m - r g_{mem} (\sigma_p - 4\sigma_m)}{(\sigma_p + 2\sigma_m)(\sigma_m^{-1} - \sigma_p^{-1})} - g_{mem}^2 r^2} \quad (4)$$

17 where  $C_{mem}$  is the capacitance per unit area of the plasma membrane;  $\sigma_m$ , the  
 18 conductivity of the external medium;  $\sigma_p$ , the internal cytoplasmic conductivity of the

1 particle; and  $g_{mem}$ , the specific membrane conductance.  $f_{co}$  is linearly dependent on the  
2 medium conductivity when the membrane conductivity is low and the cell  
3 cytoplasmic conductivity is much higher than the medium conductivity<sup>39</sup>. At  
4 frequencies higher than  $\sigma_m/C_{mem}$  and below 1 MHz, the crossover frequency of a  
5 spherical cell under these conditions can be approximated as<sup>37, 38</sup>

$$6 \quad f_{co} \approx \frac{\sigma_m}{\sqrt{2\pi r} C_{mem}} \quad (5)$$

7 For a biological cell, the conductivity of the cell cytoplasm and cell membrane is  
8 much higher and much lower than that of the suspending medium, respectively. The  
9 cell will exhibit negative and positive DEP at relatively low and high frequencies,  
10 respectively<sup>29, 38</sup>.

11

12 To produce a long-range electric field gradient with a long residence time inside  
13 the fluidic channel in order to continuously separate blood cells and cancer cells, we  
14 designed and fabricated inclined channel walls forming a V-shaped microchannel. An  
15 electric field was generated across the entire microfluidic channel between the top and  
16 the bottom conductive surfaces, and thus, a lateral electric field gradient was  
17 generated by the different distances between the top and the bottom potential sources  
18 (Figure 2(a)). When an AC voltage was applied to the top planar and bottom V-shaped  
19 conductive surfaces of the entire microchannel, it produced varied electric field

1 strengths along the  $y$ -direction in the triangular fluid chamber, thus generating a  
 2 long-range electric field gradient. Therefore, LDEP forces were induced on the  
 3 particle to produce lateral displacements normal to the continuous through-flow.  
 4 Unlike the isolated electrodes, the gradient of the electric field and the DEP force are  
 5 both sustained for the entire long channel. By doing so, target cells can be isolated in  
 6 one part of the channel, either to the middle or to the sides, depending on the particle  
 7 size and applied frequency. Balancing the DEP force with viscous drag for a particle  
 8 of size  $r$  in a medium with viscosity  $\eta$  provides a linear LDEP particle velocity normal  
 9 to the through-flow given as

$$10 \quad V_{DEP}(y) = \frac{r^2 \epsilon_m \operatorname{Re}[f_{CM}(\omega)] \nabla E^2(y)}{3\eta} \quad (6)$$

11 The DEP force strongly depends on the volume of the particle ( $F_{DEP} \sim r^3$ ) and the  
 12 gradient of the applied electric field. Therefore, the DEP mechanism can be used for  
 13 precise size separation. Based on equation (3), the LDEP velocity also depends on the  
 14 applied voltage, frequency, and particle size and the dielectric properties. The  
 15 equilibrium position of a cell is at the position where the induced particle DEP force  
 16 balances the viscous drag force in the  $y$ -direction. Therefore, the final equilibrium  
 17 position of each cell population depends on the cell DEP strength that is induced by  
 18 the electric field gradient in the  $y$ -direction.

19

## 1 **Experimental setup and microfabrication**

2 An AC voltage was supplied by a multi-output waveform generator (Wavetek,  
3 model 195) that was applied to the DEP-based microfluidic chip to induce the LDEP  
4 forces. Two portable peristaltic fluid pumps (LongerPump®, BT100-2J) were used to  
5 continuously inject the sample and buffer flows in 1:3 ratio through a 10-mL fluid  
6 chamber. The experiment was observed through an inverted fluorescence microscope  
7 (IX71, Olympus), and the experimental results were recorded in both video and photo  
8 formats using a CCD camera (30 frames/s, *Microfire*, OPTRONICS). The particle  
9 velocities and their final positions were analysed using Image-Pro Plus 6.0 software  
10 (MediaCybernetics).

11 A 1- $\mu\text{m}$ -thick silicon nitride ( $\text{Si}_3\text{N}_4$ ) layer was deposited on a Si-wafer with a  
12 crystallographic plane of 110. A positive photoresist, AZ 5214, was patterned on  $\text{Si}_3\text{N}_4$   
13 by a standard photolithography technique, and then, the exposed  $\text{Si}_3\text{N}_4$  was etched  
14 using inductively coupled plasma dry etching. The patterned  $\text{Si}_3\text{N}_4$  layer on the  
15 Si-wafer served as a passive mask during the KOH etching of the silicon. After the  
16 anisotropic wet-etching of the silicon wafer, sidewalls with  $35^\circ$  inclination were  
17 formed in the microchannel to form a V-shaped microchannel with  $110^\circ$  angle,  
18 200- $\mu\text{m}$  depth, and 700- $\mu\text{m}$  width. Titanium (Ti, 40 nm) was deposited on the formed  
19 microchannel as an adhesion layer, and gold (Au, 200 nm) was subsequently

1 deposited on the Ti layer to serve as a conductive layer by an electron beam  
2 evaporator. Figure 1(b) shows an SEM image of the V-shaped conductive  
3 microchannel. The metallic microgroove was bonded with an ITO-coated glass slide  
4 using 10- $\mu\text{m}$ -thick 3M double-sided tape to form the 3D LDEP device. The chip does  
5 not need to be patterned with the electrode geometry. Figure 1(c) shows the cross  
6 section of the microfluidic chip assembly. The chip has a face-to-face electrode  
7 configuration, a planar ITO electrode at the top, and a V-shaped groove with an  
8 Au-covered surface at the bottom of the channel to form a triangular fluid chamber.  
9 When an AC voltage was applied to the top planar and bottom V-shaped conductive  
10 surfaces, varied electric field strengths were generated along the y-direction to  
11 produce an electric field gradient along the entire channel (Figure 2(a)). The  
12 fabrication processes for the 3D LDEP chips are relatively simple and do not require  
13 expensive equipment and time-consuming procedures as is the case with the  
14 electroplating-based 3D DEP chips and face-to-face DEP gates<sup>27, 32</sup>. The 3D metallic  
15 microchannel used to drive the DEP forces can be fabricated in three simple  
16 steps—microchannel fabrication, metal deposition, and chip bonding—thus  
17 eliminating the need for electrode patterning and precise alignment steps in the top  
18 and bottom layers.  
19

## 1 **Sample preparation**

2 To easily distinguish the tumour cells from the blood cells by fluorescent  
3 microscopy, a GFP-expressing human lung adenocarcinoma cell line,  
4 PC14PE6/AS2-GFP (AS2-GFP), was used to study the separation capability and  
5 isolation efficiency of the proposed chip. We had previously established this cell line  
6 by stably transfecting the parental AS2 cells with GFP-expressing plasmid<sup>40</sup>. The  
7 AS2-GFP cells were maintained in MEM- $\alpha$  (Invitrogen, Carlsbad, CA, USA) with  
8 10% foetal calf serum (FCS; Invitrogen) and incubated at 37°C in a humidified  
9 atmosphere containing 5% CO<sub>2</sub>.

10 To investigate the isolation capability, the AS2-GFP cells were seeded 48 h  
11 before the experiments. The cells were grown to subconfluent densities and collected  
12 using trypsin. The trypsin was then neutralized using an FCS-supplemented medium.  
13 The cells were washed once and resuspended with the FCS-supplemented medium.

14 Leukocytes (WBCs) and erythrocyte (RBCs) were isolated from whole blood  
15 using Ficoll-Paque (GE Healthcare Life Sciences) density gradient separation for  
16 individually investigating the DEP properties of WBCs and RBCs. 3 mL of blood  
17 from a healthy human was carefully added to 3 mL of Ficoll buffer, and then, the  
18 sample was centrifuged at 2100 rpm for 20 min at 20–25°C. After centrifugation, the  
19 buffy coat of the PBMC and RBC were carefully taken out and individually

1 resuspended in the PBS buffer. Then, the cells were washed two times using the  
2 experimental buffer. Finally, the WBCs and RBCs were individually resuspended in 3  
3 mL of the experimental buffer to further investigate the DEP behaviours. The final  
4 WBC and RBC concentrations were adjusted to  $\sim 5 \times 10^5$  cells/mL and  $5 \times 10^6$   
5 cells/mL, respectively.

6 An isotonic phosphate buffered saline (PBS) buffer diluted with 280 mM sucrose  
7 in 1:20 ratio ( $\sigma_m \sim 0.78$  mS/cm) was used as the experimental buffer because human  
8 cells are highly sensitive to the osmotic pressure of a solution. Human blood cells  
9 were diluted 20 times ( $\sim 2.3 \times 10^8$  cells/mL) using the experimental buffer to avoid  
10 blood cell coagulation. The diluted blood samples were spiked with cancer cell  
11 concentrations of  $6 \times 10^2$ ,  $3 \times 10^3$ , and  $3 \times 10^4$  cells/mL to investigate the separation  
12 capability in the 3D LDEP platform.

13

#### 14 **Evaluation of purity and recovery rate of tumour cell isolation**

15 We used two different methods to determine the cell concentrations and  
16 tumour/blood ratios in the samples and sorted products. First, the samples were  
17 evaluated using a Countess automated cell counter (Invitrogen) according to the  
18 manufacturer's instructions. Briefly, 6  $\mu$ L of the cell-containing sample was taken and  
19 mixed with trypan blue in 1:1 ratio. Then, 10  $\mu$ L of the mixture was loaded into a



1 counting slide chamber, and the cells were counted in the automated cell counter. A  
2 single sample measurement using this counter provided the following data: total cell  
3 concentration, cell viability, viable cells : total cells ratio, and cell size. After  
4 automated cell counting, we further subjected the counting slide to fluorescent  
5 microscopy analysis. The cells were counted in five random fields at 100x  
6 magnification under a Nikon Eclipse Ti fluorescent microscope with both bright light  
7 and green fluorescent images. We also subjected the samples to further fluorescence  
8 microscopy analysis.

9

## 10 **Results and Discussions**

### 11 **Chip design and finite element simulation**

12 Finite element simulations were conducted to predict the electric field  
13 distribution and its magnitude. They were solved numerically using finite element  
14 analysis software (Comsol Multiphysics 3.5, Comsol Ltd.). The electric scalar  
15 potential  $V$  satisfies Poisson's equation. The electric field and displacement were  
16 obtained from the gradient of  $V$ .

17 The short-range and local distribution of the electric field gradient is a key  
18 limitation for DEP-based manipulation techniques. Even when the field gradient was  
19 increased greatly through micro-/nanofabrication, the long-range manipulation of

1 particles was difficult to achieve in DEP separation systems. Our proposed 3D  
2 V-shaped electrode configuration provides a long-range field gradient in the entire  
3 channel. Figure 2(a) shows the electric field distribution for the proposed design. The  
4 field maxima locate at the channel side walls, and the field minima locate in the  
5 middle of the channel; this is because the electrode separation distance between the  
6 top and the bottom layers gradually decreases from the sidewalls of the channel to the  
7 middle region (Figure 2(b)). Therefore, the directions of the negative DEP force are  
8 toward the centre region of the channel, as shown in Figure 2(b). In Figure 2(b), the  
9 arrows represent the directions of the normalized negative electric field gradient  
10 (direction of negative DEP force). In addition, the V-shaped and trapezoid metallic  
11 channels were used to compare the geometrical effect of the electric field distribution.  
12 The design of the trapezoid channel shows that the electric field distribution has two  
13 second minima field regions near the lower line, as shown in the supplementary  
14 material. On the other hand, the V-shaped design only has one minima field region in  
15 the middle of the channel (Figure 2(b)). Therefore, a triangular configuration may be  
16 more suitable for the negative DEP-based separation strategy. Compared to a 2D  
17 planar electrode-based DEP, the 3D electric field gradient design also minimizes  
18 decays in the DEP force, such that both forces increase monotonically with voltage to  
19 further increase the throughput.

1

## 2 **Lateral Migration Velocities and Equilibrium Positions**

3       The DEP velocity spectra of RBC, WBC, and AS2-GFP cells were investigated  
4 to determine the appropriate frequencies for effectively separating cancer cells and  
5 blood cells in a continuous through-flow. The velocity was calculated by measuring  
6 the time taken for individual cells to move a given distance from the channel side wall  
7 toward an equilibrium position (negative LDEP) or a distance from a position toward  
8 the channel side wall (positive LDEP), with a time interval of 0.1 s/frame. Figure 3(a)  
9 shows the measured results of cell velocity versus applied frequency when a constant  
10 voltage of 20 V<sub>pp</sub> was applied. The velocity profiles indicate that the cells induced a  
11 negative and a positive DEP force at relatively low and relatively high frequencies,  
12 respectively. The cross-over frequency of RBC, WBC, and AS2-GFP cells was  
13 measured at 600–700, 300–400 and 100–200 kHz, respectively. High differences  
14 occurred in the LDEP velocity between the AS2-GFP cells and the blood cells at  
15 frequencies lower than 50 kHz and higher than 400 kHz. To avoid cell adhesion to the  
16 channel surface at high frequencies (positive DEP) and bobble generation at low  
17 frequencies (lower than 2 kHz), a frequency of 10 kHz was chosen for future  
18 investigations and cell separation.

19       The DEP velocity increases/decreases with a square relationship of the electric

1 field gradient and particle size. Therefore, the large difference in the particle size of  
2 cancer cells and blood cells could induce different lateral migration velocities and  
3 cause stopping at different equilibrium positions under a predetermined electrical  
4 condition. Therefore, the appropriate frequencies for the separation of AS2-GFP cells,  
5 WBCs, and RBCs were first investigated, and a frequency of 10 kHz was set to  
6 measure the equilibrium positions of these three types of cells. Cell equilibrium  
7 occurs at the position where the particle DEP force balances the fluid viscous force in  
8 the microchannel. In our design, the electric field strength gradually reduces from the  
9 channel side walls toward the centre of the microchannel. The results show that the  
10 equilibrium positions are very different in the cancer cells and blood cells owing to  
11 the different cell sizes, causing a difference in their corresponding threshold DEP  
12 forces at different positions in the y-direction (AS2-GFP: 15–25  $\mu\text{m}$ , WBC: 8–12  $\mu\text{m}$ ,  
13 RBC: 6–8  $\mu\text{m}$ <sup>38</sup>). The result also showed that the induced LDEP velocity increased  
14 with the applied AC voltage (Figure 3(b)), and the equilibrium positions presented  
15 toward the middle of the channel when the applied voltage increased, as shown in  
16 Figure 3(c). The results show that the equilibrium positions of WBCs and RBCs are  
17 very close, and their experimental images are very similar. Therefore, we only showed  
18 the equilibrium position images of blood cells and AS2-GFP cells to highlight their  
19 differences (Figure 3(c1) and (c2)). Considering the equilibrium positions and

1 equilibrium time (Figure 3(b) and (c)), an optimal separation situation is given as

$$2 \quad t_{DEP\_BC(y)} > t_{flow(x)} > t_{DEP\_CTC(y)} \quad (7)$$

3 Here,  $t_{flow}$  is the characteristic time required for the sample flow to pass through the

4 length of the flowing channel  $l$ ,  $t_{flow} = l/v_{flow}(x)$ , and  $t_{DEP}$  is the characteristic time

5 as defined by the required time to transport a specific cell from an initial position to

6 the equilibrium position by a distance  $d$ ,  $t_{DEP} = d/v_{DEP}(y)$ .  $v_{flow}(x)$  and  $v_{DEP}(y)$

7 are the sample flow velocity along the x-direction and the induced cell DEP velocity

8 along the y-direction, respectively. The separation distance between the two types of

9 cells can be defined as  $d_{separation} = |(d_{eq1} - v_{DEP1} \times t_{flow}) - (d_{eq2} - v_{DEP2} \times t_{flow})|$ , where

10  $d_{eq1}$  and  $d_{eq2}$  is the equilibrium position for cell 1 and cell 2, respectively. Therefore,

11 the optimal separation situation depends on the particle residence time in the DEP

12 field versus the flow transition time and the differences in the equilibrium positions

13 between the CTC and the blood cells.

14

### 15 **Continuous sorting of cancer cells from blood**

16 The sample and buffer flow rates were applied in 1:3 ratio, and thus, the sample

17 flow with the suspended cancer cells and blood cells can both be collected as two

18 particle streams along the side walls of the channel. Under this condition, the flowing

19 sample stream involving blood cells and AS2-GFP cells can be collected at a distance

1 of 150–200  $\mu\text{m}$  from the channel side walls (Figure 4(a)). The AS2-GFP cells and  
2 blood cells both flowed into the upper and lower subchannels when no electric field  
3 was applied (Figure 4(b)). In this DEP microfluidic chip, the fluorescent AS2-GFP  
4 cells and blood cells flowed along the x-direction of a 6-cm-long channel, and an  
5 external AC electric field (an applied voltage of 18  $V_{pp}$  at a frequency of 10 kHz) was  
6 applied to produce DEP forces perpendicular to the flow direction (along the  
7 y-direction). When the flowing cells entered the LDEP field regions, a negative LDEP  
8 force pushed them toward the centre of the channel. Here, the AS2-GFP cells  
9 experienced a higher LDEP force that induced a longer lateral displacement to be  
10 manipulated into the middle region of the channel, as shown in Figure 4(c). On the  
11 other hand, the blood cells experienced a lower LDEP force that induced shorter  
12 displacements, and they could only be moved a distance of  $\sim 200 \mu\text{m}$  from the channel  
13 side walls (Figure 4(c)). These effects resulted in the separation of the CTCs and  
14 blood cells into the middle and upper/lower subchannels, respectively, as shown in  
15 Figure 4(d). The figure shows very dense blood cells ( $\sim 2.3 \times 10^8$  cells/mL) in the  
16 input sample wherein the AS2-GFP cells ( $\sim 1200$  CTCs/mL) are difficult to count and  
17 further analyse precisely (Figure 5(a) and (b)) because dense blood cells could hide  
18 the AS2-GFP cells and significantly interfere with the downstream molecular analysis.  
19 After the LDEP isolation, the sorted sample showed that the blood cells were greatly

1 reduced (roughly 4–5 orders of blood cells removed), as shown in Figure 5(b) and (c),  
2 and the number of CTCs could be counted and further analysed easily. Crystal violet  
3 staining showed that the viability of the isolated cancer cells reached ~85% (data not  
4 shown).

5 In a high-ionic-strength fluid, the electrothermal effect near the microelectrodes  
6 was also taken into consideration. The increase in the local temperature induced by  
7 the applied AC electric field can be calculated by  $\Delta T \sim \sigma V_{\text{rms}}^2 / k$ <sup>41</sup>. For the applied  
8 voltage of 18 V<sub>pp</sub>, frequency of 5 kHz to 1 MHz, medium conductivity of 0.78 mS/cm,  
9 and thermal conductivity of k (1.0 W/mK), the temperature rise can be estimated to be  
10 only ~6.2°C. In addition, a continuous through-flow separation system can reduce the  
11 Joule thermal effect near the electrode surface<sup>42</sup> owing to through-flow convection,  
12 especially when the flow passes through a high-thermal-conductivity material such as  
13 silicon<sup>38</sup>. Therefore, the separation process in the continuous flow chamber would not  
14 be influenced significantly. Furthermore, a negative DEP force from the top and  
15 bottom electrodes can also minimize sedimentation and field-induced lysis of the cells  
16 <sup>43</sup>.

17

### 18 **Recovery rate and isolation purity**

19 The recovery rate is defined as the percentage of the isolated cancer cell number

1 over the initial spiked cancer cell number in the prepared blood sample. The  
2 predetermined optimal condition (18 V<sub>pp</sub> at 10 kHz) was applied to a 6-cm-long LDEP  
3 channel wherein different flow rates were used to investigate the isolation  
4 performance. Figure 6(a) shows that the recovery rate can reach as high as 84%–92%  
5 and 81%–88% at a flow rate of 10 and 20 μL/min, respectively. Furthermore, as the  
6 flow rate increases to 30 μm/min, the recovery rate decreases significantly to ~60%.  
7 This result could be attributed to the fact that the cell transportation time in the  
8 through-flow is shorter than the characteristic LDEP time when the flow rate is higher  
9 than 20 μL/min. The experimental results also indicate that the cell concentration does  
10 not significantly influence the isolation recovery. The experimental results show that  
11 an isolation purity of 81.6%, 91.3%, and 87% was achieved at a flow rate of 10, 20,  
12 and 30 μL/min, respectively, when the original cancer cell purity was 0.01% (Figure  
13 6(b)). Therefore, the results show an excellent enrichment factor of ~10<sup>5</sup> in our LDEP  
14 sorter. In our observation, a higher flow rate leads to a higher capability for blood cell  
15 depletion. However, the recovery also decreased significantly when the flow rate was  
16 as high as 30 μL/min. The coupled effects resulted in lower isolation purity compared  
17 to that under the optimal flow rate of 20 μL/min (Figure 6(b)). Considering the high  
18 isolation purity, recovery, and throughput, the recommended flow rate for LDEP CTC  
19 isolation was set at 20 μL/min to achieve high enrichment of 10<sup>5</sup> and high recovery



1 rate greater than 85%.

2 Ideally, the proposed separation strategy involves increasing the channel length  
3 to effectively increase the throughput. Therefore, to prove this concept, a 13-cm-long  
4 serpentine DEP channel was used to isolate cancer cells from the diluted blood at a  
5 higher flow rate of 40  $\mu\text{L}/\text{min}$ . Figure 6(c) shows the isolation recovery at flow rates  
6 of 20 and 40  $\mu\text{L}/\text{min}$  using a 6- and 13-cm-long LDEP channel, respectively. The cells  
7 in a 6-cm-long LDEP microchannel experienced a shorter particle residence time in  
8 the DEP field, and the experimental results show that the recovery decreased  
9 significantly when the flow rate was increased to 40  $\mu\text{L}/\text{min}$ . On the other hand, the  
10 cells in a 13-cm-long DEP microchannel experienced a longer LDEP affecting time,  
11 and thus, the recovery reached ~81% and only decreased slightly (<10%) when the  
12 flow rate increased up to 40  $\mu\text{L}/\text{min}$ . The results confirm that the proposed isolation  
13 strategy can increase the isolation throughput by increasing the particle residence time  
14 in the LDEP field, which is in good agreement with the numerical predictions.

15

## 16 **Conclusions**

17 We have extensively characterized the proposed LDEP-based microfluidic chip  
18 by varying the applied AC voltage, frequency, sample flow rate, and length effect of  
19 the LDEP channel and optimizing these parameters for the isolation purity, recovery,

1 and throughput. Compared to conventional physical methods (purity = ~0.5%–10%),  
2 immunomagnetism-based methods, and microfluidic biomarker-based methods, the  
3 isolation purity, recovery rate, throughput, and viability of the proposed antibody-free  
4 chip were excellent, especially with regard to high enrichment at high flow rate (>20  
5  $\mu\text{L}/\text{min}$ ). The recovery was greater than 85%, and the isolation purity was greater than  
6 90% when the original cancer cell purity was 0.01% (enrichment factor:  $\sim 10^5$ ). The  
7 great advantage of this separation strategy is that increasing the channel length to  
8 prolong the particle residence time in the LDEP field can effectively increase the  
9 throughput proportionally. For proof of the proposed concept, 2.4 mL/h isolation  
10 throughput with a recovery rate as high as 81% was achieved within a 13-cm-long  
11 LDEP-based microchannel. Under this condition, a 5 mL sample volume could be  
12 isolated in  $\sim 2$  h, and blood cells could be removed with a depletion rate of  $10^5$ .  
13 On-chip analysis of the isolated cells is ongoing and expected to be applicable for  
14 many detection approaches such as electrical and optical spectra analysis approaches.

15  
16

### 17 **Acknowledgements**

18 This work was supported by the Ministry of Science and Technology of Taiwan  
19 (MOST 102-2221-E-492-001-MY2, MOHW 103-TD-B-111-06 and  
20 MOHW103-TDU-B-211-113002). We also thank the National Nano Device  
21 Laboratory for supplying the micro-fabrication equipment.

22  
23  
24

## 1   **References**

- 2   1. V. Zieglschmid, C. Nollmann and O. Bocher, *Crit. Rev. Clin. Lab.*, 2005, **42**, 155.
- 3   2. L. Yu, S. R. Ng, Y. Xu, H. Dong, Y. J. Wang and C. M. Li, *Lab Chip*, 2013, **13**,  
4   3163.
- 5   3. S. Mocellin, D. Hoon, A. Ambrosi, D. Nitti and C. R. Rossi, *Clin. Cancer Res.*,  
6   2006, **12**, 4605.
- 7   4. Z. S. Lalmahomed, J. Kraan, J. W. Gratama, B. Mostert, S. Sleijfer and C. Verhoef,  
8   *J. Clin. Oncol.*, 2010, **28**, 288.
- 9   5. S. M. B. Fong, M. K. Lee, P. S. Adusumilli and K. J. Kelly, *Surgery*, 2009, **146**,  
10   498.
- 11   6. P. K. Y. Goon, C. J. Boos, P. S. Stonelake, A. D. Blann, G. Y. H. Lip, *Thromb.*  
12   *Haemost.*, 2006, **96**, 45-52.
- 13   7. G. Deng, M. Herrler, D. Burgess, E. Manna, D. Krag and J. F. Burke, *Breast*  
14   *Cancer Res.*, 2008, **10**, 69.
- 15   8. F. I. Thege, T. B. Lannin, T. N. Saha, S. T., M. L. Kochman, M. A. Hollingsworth,  
16   A. D. Rhim and B. J. Kirby, *Lab Chip*, 2014, **14**, 1775.
- 17   9. S. Wang, H. Wang, J. Jiao, K.-J. Chen, G. E. Owens, K. Kamei, J. Sun, D. J.  
18   Sherman, C. P. Behrenbruch, H. Wu and H.-R. Tseng, *Angew. Chem. Int. Ed.*,  
19   2009, **48**, 8970.
- 20   10. S. Nagrath, L. V. Sequist, S. Maheswaran, D. W. Bell, D. Irimia, L. Ulkus, M. R.  
21   Smith, E. L. Kwak, S. Digumarthy, A. Muzikansky, P. Ryan, U. J. Balis, R. G.  
22   Tompkins, D. A. Haber and M. Toner, *Nature*, 2007, **450**, 1235.
- 23   11. J. Xia, X. Chen, C. Z. Zhou, Y. G. Li and Z. H. Peng, *IET Nanobiotechnol.*, 2011,  
24   5, 114–120.
- 25   12. T. Ohnaga, Y. Shimada, M. Moriyama, H. Kishi, T. Obata, K. Takata, T. Okumura,  
26   T. Nagata, A. Muraguchi and K. Tsukada, *Biomed. Microdevices*, 2013, **15**, 611.
- 27   13. W. Chen, S. Weng, F. Zhang, S. Allen, X. Li, L. Bao, R. H. W. Lam, J. A.  
28   Macoska, S. D. Merajver and J. Fu, *ACS nano*, 2013, **7**, 566.
- 29   14. J. H. Kang, S. Krause, H. Tobin, A. Mammoto, M. Kanapathipillai and D. E.  
30   Ingber, *Lab Chip*, 2012, **12**, 2175.
- 31   15. S. D. Mikolajczyk, L. S. Millar, P. Tsinberg, S. M. Coutts, M. Zomorodi, T.

- 1 Pham, F. Z. Bischoff and T. J. Pircher, *Oncology*, 2011, **10**, 252361.
- 2 16. P.T.H. Went, A. Lugli, S. Meier, M. Bundi, M. Mirlacher, G. Sauter and S.  
3 Dirnhofer, *Hum. Pathol.*, 2004, **35**, 122.
- 4 17. I. Cima, C. W. Yee, F. S. Iliescu, W. M. Phyto, K. H. Lim, C. Iliescu and M. H.  
5 Tan, *Biomicrofluidics*, 2013, **7**, 011810.
- 6 18. A. Karimi, S. Yazdi and A. M. Ardekani, *Biomicrofluidics*, 2013, **7**, 021501.
- 7 19. H. Mohamed, L. D. McCurdy, D. H. Szarowski, S. Duva, J. N. Turner and M.  
8 Caggana, *IEEE Trans. Nanobiosci.*, 2004, **3**, 251.
- 9 20. S. J. Tan, R. L. Lakshmi, P. F. Chen, W. T. Lim, L. Yobas and C. T. Lim, *Biosens.*  
10 *Bioelectron.*, 2010, **26**, 1701.
- 11 21. A. A. S. Bhagat, H. W. Hou, L. D. Li, C. T. Lim and J. Y. Han, *Lab Chip*, 2011,  
12 **11**, 1870.
- 13 22. H. W. Hou, M. E. Warkiani, B. L. Khoo, Z. R. Li, R. A. Soo, D. S.-W. Tan, W.-T.  
14 Lim, J. Han, A. A. S. Bhagat and C. T. Lim, *Sci. Rep.*, 2013, **3**, 1259.
- 15 23. A. J. Mach, J. H. Kim, A. Arshi, S. C. Hurab and D. D. Carlo, *Lab Chip*, 2011, **11**,  
16 2827.
- 17 24. H.-S. Moon, K. Kwon, S.-I. Kim, H. Han, J. Sohn, S. Lee and H.-I. Jung, *Lab*  
18 *Chip*, 2011, **11**, 1118.
- 19 25. I-F. Cheng, H.-C. Chang, T.-Y. Chen, C. Hu and F.-L. Yang, *Sci. Rep.*, 2013, **3**,  
20 2365.
- 21 26. K.-H. Han, S.-I. Hana and A. B. Frazier, *Lab Chip*, 2009, **9** 2958.
- 22 27. T. Müller, A. Pfennig, P. Klein, G. Gradl, M. Jäger, and T. Schnelle, *IEEE Eng.*  
23 *Med. Biol. Mag.*, 2003, **22**, 51.
- 24 28. M. Alshareef, N. Metrakos, E. J. Perez, F. Azer, F. Yang, X. Yang and G. Wang,  
25 *Biomicrofluidics*, 2013, **7**, 011803.
- 26 29. I-F. Cheng, C.-C. Lin, D.-Y. Lin and H.-C. Chang, *Biomicrofluidics*, 2010, **4**,  
27 034104.
- 28 30. S.-B. Huang, M.-H. Wu, Y.-H. Lin, C.-H. Hsieh, C.-L. Yang, H.-C. Lin, C.-P.  
29 Tseng and G.-B. Lee, *Lab Chip*, 2013, **13**, 1371.
- 30 31. I-F. Cheng, S.-L. Liu, C.-C. Chung and H.-C. Chang, *Microfluid Nanofluid*, 2012,

- 1        **12**, 95.
- 2    32. G. Mernier, E. Duqi and P. Renaud, *Lab Chip*, 2012, **12**, 4344.
- 3    33. I-F. Cheng, V. Froude, Y.-E. Zhu, H.-C. Chang and H.-C. Chang, *Lab Chip*, 2009,  
4        **9**, 3193.
- 5    34. Y. Huang, X. B. Wang, J. A. Tame and R. Pethig, *J. Phys. D: Appl. Phys.*, 1993,  
6        **26**, 1528.
- 7    35. V. Gupta, I. Jafferji, M. Garza, V. O. Melnikova, D. K. Hasegawa, R. Pethig and  
8        D. W. Davis, *Biomicrofluidics*, 2012, **6**, 024133.
- 9    36. S. Bose, R. Singh, M. Hanewich-Hollatz, C. Shen, C.-H. Lee, D. M. Dorfman, J.  
10       M. Karp and R. Karnik, *Sci. Rep.*, 2013, **3**, 2329.
- 11   37. J. Gimsa, P. Marszalek, U. Loewe, and T. Y. Tsong, *Biophys. J.*, 1991, **60**, 749.
- 12   38. P. R. C. Gascoyne, S. Shim, J. Noshari, F. F. Becker and K. Stemke-Hale,  
13        *Electrophoresis*, 2013, **34**, 1042.
- 14   39. J. Gimsa, M. Stubbe, and U. Gimsa, *J. Electr. Bioimp.*, 2014, 5, 74.
- 15   40. H. H. Yeh, W. W. Lai, H. H. Chen, H. S. Liu, W. C. Su, *Oncogene*, 2006 , **25**,  
16        4300.
- 17   41. C. Rosales, *Electrophoresis*, 2006, **27**, 1984.
- 18   42. C. Iliescu, G. L. Xu, V. Samper and F. E. H. Tay, *J. Micromech. Microeng.*, 2005,  
19        **15**, 494.
- 20   43. P. R. C. Gascoyne, J. Noshari, T. J. Anderson and F. F. Becker, *Electrophoresis*,  
21        2009, **30**, 1388.

### Figure captions

26    Figure 1 The LDEP CTC isolation system. (a) The induced LDEP forces on the blood  
27    cells and CTC produce different LDEP velocities normal to the through-flow and  
28    balance the fluid viscosity at different equilibrium positions, resulting in the sorting of  
29    CTCs and blood cells to different downstream subchannels. (b) SEM image of a  
30    V-shaped conductive microchannel. (c) Cross-sectional diagram of the microfluidic  
31    chip assembly.

1 Figure 2 Finite element simulation of electric field for 3D V-shaped and trapezoid  
2 electrode configurations. (a) The electric field was generated across the entire  
3 microfluidic channel between the top and the bottom conductive surfaces, and  
4 therefore, it provides a long-range field gradient in the entire channel. (b) The lateral  
5 electric field gradient was generated by the different distances between the top and the  
6 bottom potential sources, and the V-shaped design only has one minima field region  
7 in the middle of channel.

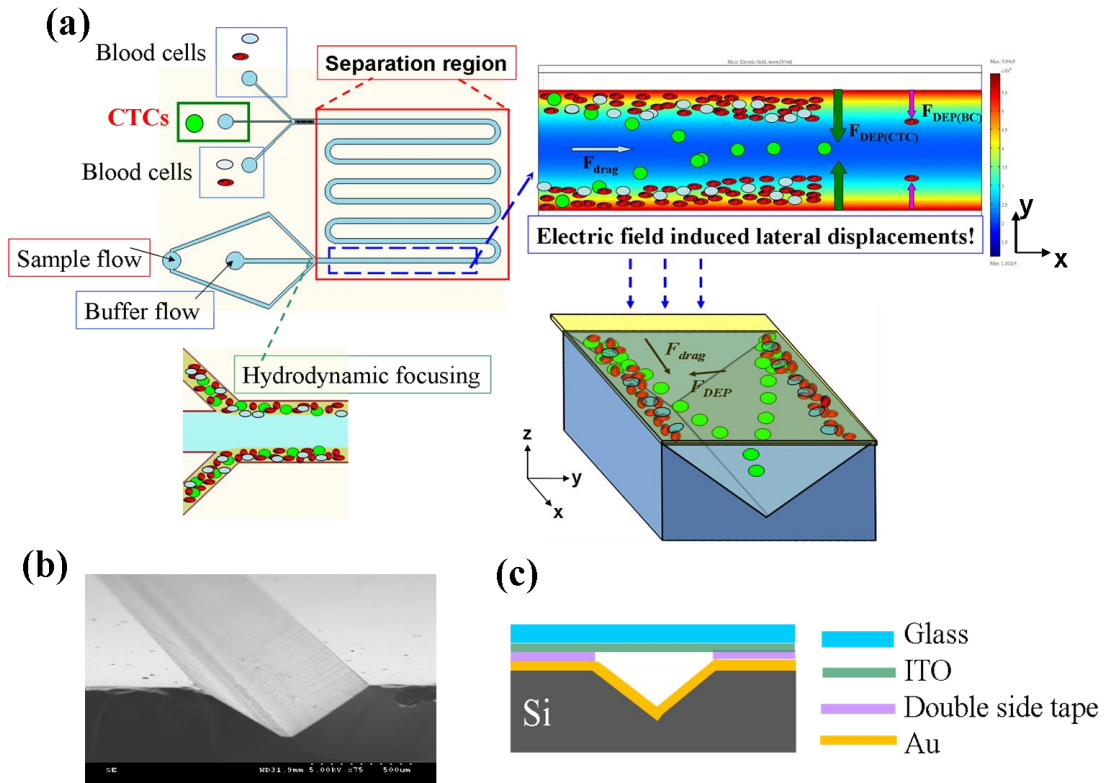
8  
9 Figure 3 (a) Experimentally determined LDEP velocity–frequency profile showing the  
10 appropriate range of applied frequencies for blood cell and CTC separation (data are  
11 averaged over three runs). (b) LDEP moving velocity of AS2-GFP, WBCs, and RBCs  
12 versus various applied voltages. (c) Various applied voltages versus the related  
13 equilibrium positions for RBCs, WBCs, and AS2-GFP cells, respectively.

14  
15 Figure 4 (a) The flowing sample stream involving blood cells and AS2-GFP cells was  
16 collected at a distance of 150–200  $\mu\text{m}$  from the channel side walls using  
17 hydrodynamic focusing. (b) Both cancer cells and blood cells flowed into the upper  
18 and lower subchannels when no electric field was applied. (c) When a determined  
19 electric field was applied, AS2-GFP cells experienced a higher LDEP force that  
20 induced a longer lateral displacement to be manipulated into the middle region of the  
21 channel. Blood cells experienced a lower LDEP force that induced a shorter  
22 displacement, and they were only transported to a distance of  $\sim 200 \mu\text{m}$  from the  
23 channel side walls. (d) Separation of cancer cells and blood cells into the middle and  
24 upper/lower subchannels, respectively.

25  
26 Figure 5 (a) Very dense blood cells and rare AS2-GFP cells in the input sample,  
27 wherein the AS2-GFP cells are difficult to examine. (b) AS2-GFP cells in a very dense  
28 blood sample in a fluorescence field. (c) After DEP isolation, the sorted sample  
29 showed that the blood cells were greatly reduced. (d) Sorted AS2-GFP cells in the  
30 fluorescence field after DEP enrichment.

31  
32 Figure 6 (a) The recovery rate at different flow rates achieved by using a LDEP chip.  
33 (b) The isolation purity versus different spiked AS2-GFP concentrations at different  
34 flow rates. (c) The isolation recovery at flow rates of 20 and 40  $\mu\text{L}/\text{min}$  using a 6- and  
35 a 13-cm-long LDEP channel, respectively. The AS2-GFP cells in a 13-cm-long  
36 channel experienced a longer LDEP affecting time, and the recovery still reached  
37  $\sim 80\%$  when the flow rate increased up to 40  $\mu\text{L}/\text{min}$ .

Figure 1



1  
2  
3  
4  
5  
6  
7  
8  
9  
10  
11  
12  
13  
14  
15  
16  
17  
18  
19  
20  
21  
22  
23  
24  
25  
26  
27  
28  
29  
30  
31  
32  
33  
34  
35  
36  
37  
38

Figure 2

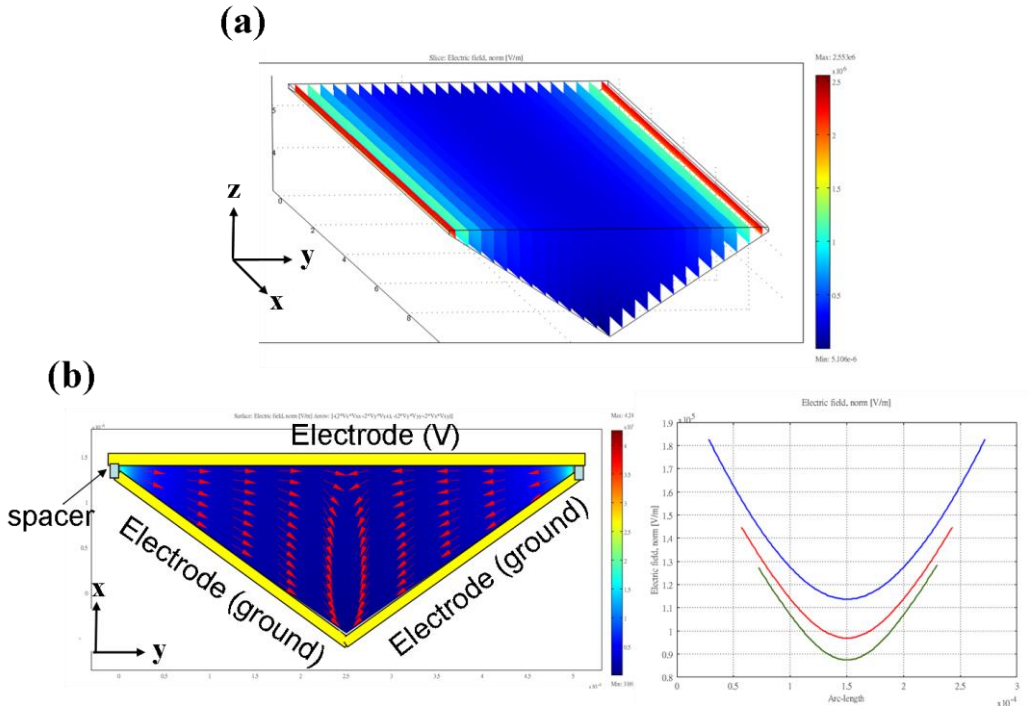
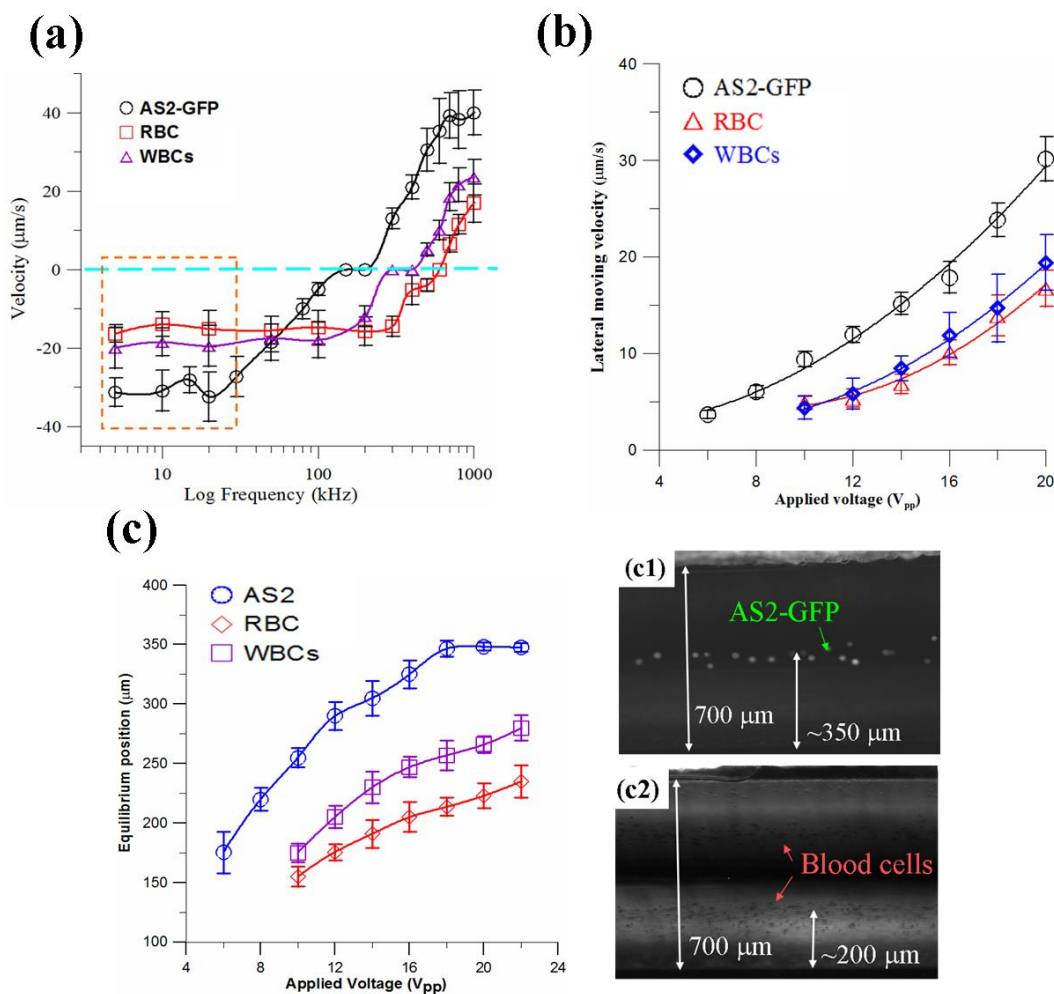




Figure 3



1  
2  
3  
4  
5  
6  
7  
8  
9  
10  
11  
12  
13  
14  
15  
16  
17  
18  
19  
20  
21  
22  
23  
24  
25  
26  
27  
28  
29  
30  
31  
32  
33  
34  
35  
36  
37  
38

Figure 4

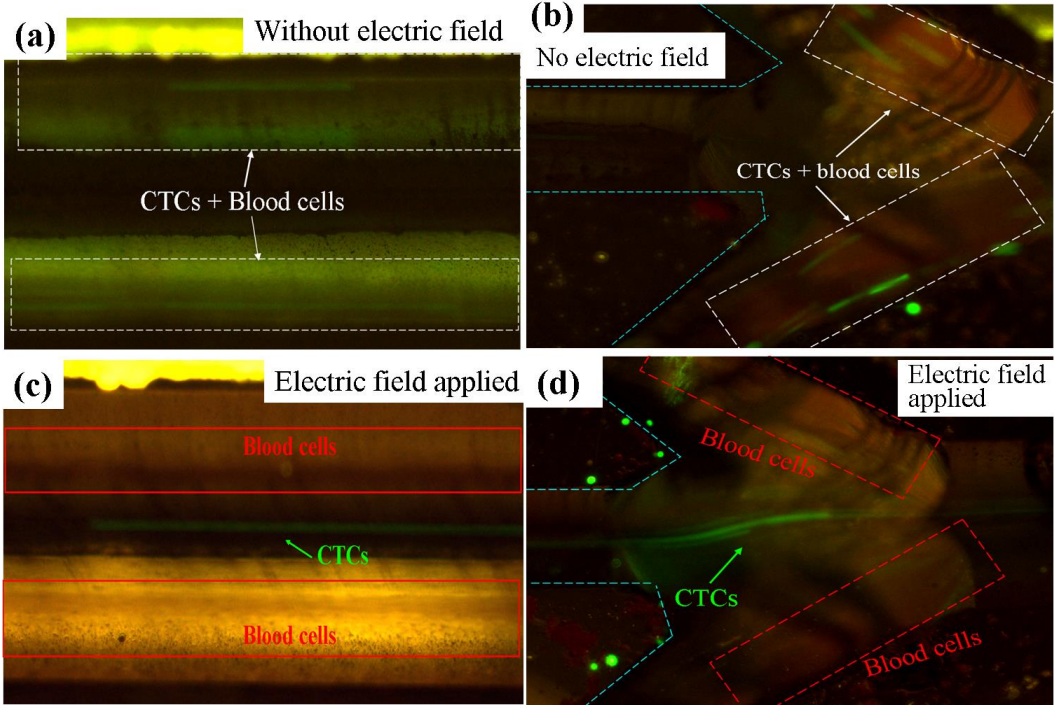


Figure 5

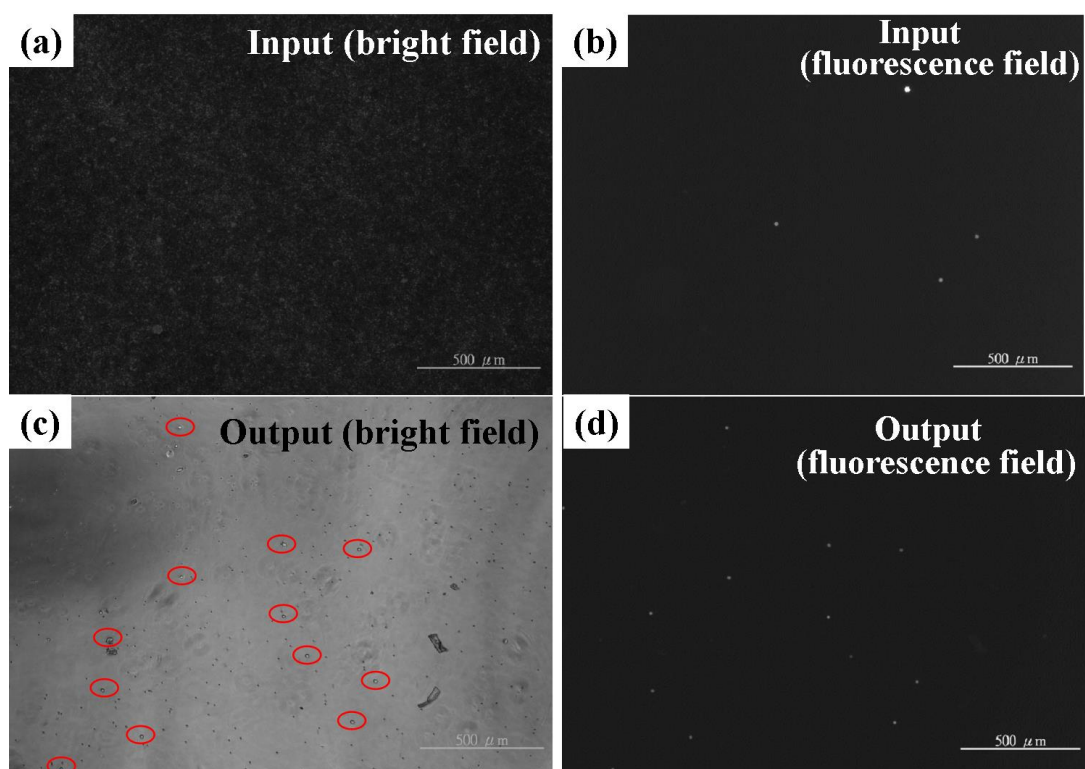


Figure 6

